ACS APPLIED ENERGY MATERIALS

www.acsaem.org
Article

Cobalt–Iron Oxyhydroxide Obtained from the Metal Phosphide: A Highly Effective Electrocatalyst for the Oxygen Evolution Reaction at High Current Densities

María Isabel Díez-García,* Guillem Montaña-Mora, Marc Botifoll, Andreu Cabot, Jordi Arbiol, Mohammad Qamar, and Joan Ramon Morante

Cite This: ACS Appl. Energy Mater. 2023, 6, 5690–5699

ABSTRACT: The development of high current density anodes for the oxygen evolution reaction (OER) is fundamental to manufacturing practical and reliable electrochemical cells. In this work, we have developed a bimetallic electrocatalyst based on cobalt–iron oxyhydroxide that shows outstanding performance for water oxidation. Such a catalyst is obtained from cobalt–iron phosphide nanorods that serve as sacrificial structures for the formation of a bimetallic oxyhydroxide through phosphorous loss concomitantly to oxygen/hydroxide incorporation. CoFeP nanorods are synthesized using a scalable method using triphenyl phosphite as a phosphorous precursor. They are deposited without the use of binders on nickel foam to enable fast electron transport, a highly effective surface area, and a high density of active sites. The morphological and chemical transformation of the CoFeP nanoparticles is analyzed and compared with the monometallic cobalt phosphide in alkaline media and under anodic potentials. The resulting bimetallic electrode presents a Tafel slope as low as 42 mV dec^{-1} and low overpotentials for OER. For the first time, an anion exchange membrane electrolysis device with an integrated CoFeP-based anode was tested at a high current density of 1 A cm^{-2}, demonstrating excellent stability and Faradaic efficiency near 100%. This work opens up a way for using metal phosphide-based anodes for practical fuel electrosynthesis devices.

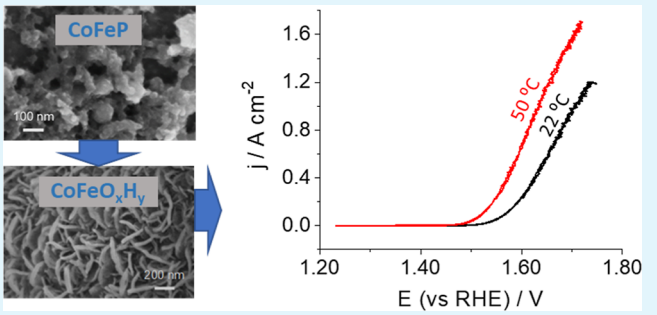

KEYWORDS: *cobalt iron phosphide, nanorods, anode, nickel foam, oxyhydroxide, anion exchange membrane*

INTRODUCTION

The production of fuels by electroconversion coupled with renewable sources is one of the backbones of a sustainable energy future. In most of these systems, such as the electrosynthesis of H_2, NH_3, or CO_2 reduction products, the corresponding cathodic reaction is usually coupled to the oxygen evolution reaction (OER). Nevertheless, OER is the most sluggish reaction in the overall process, and its complexity derives from the four reaction steps associated with this reaction. Consequently, a rational design of the anode requires strategies for overcoming this drawback. The use of multi-metallic catalysts is advantageous as they can provide appropriate metallic sites for achieving a more effective reduction of the energy barriers associated with each reaction step.[1,2] To this end, a dispersion of metallic atoms with adjacent locations in the electrode frame and skeleton should be ensured to achieve an adequate density of active sites to reach high production rates. Furthermore, this rational design of the anode must take into account its electrical conductivity to guarantee adequate electron transport, the mass transport to or from the active sites to prevent diffusion limitations, and also the kinetics associated with the reactions taking place in the active site.

The use of metal oxides as electrocatalysts generally has the limitation of their low conductivity. Among the alternative compounds reported, transition metal phosphides (TMPs) are excellent candidates as some of them present metallic-like properties and exhibit much higher conductivities[3] than the corresponding metal oxides. TMPs have attracted much interest as electrocatalysts for water splitting for both half-reactions, hydrogen evolution reaction (HER) and OER.[1,4−7] In this context, cobalt, iron, and the corresponding bimetallic phosphides have been reported as electrocatalysts for the OER, displaying low overpotentials.[1,7,8] So far, most of these studies have been focused on the electrocatalytic activity at low and

Received: January 5, 2023
Accepted: April 17, 2023
Published: May 25, 2023

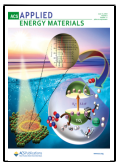

https://doi.org/10.1021/acsaem.3c00032
ACS Appl. Energy Mater. 2023, 6, 5690−5699

medium currents (10−50 mA cm^{-2}), while working at high current densities, >1 A cm^{-2}, has barely been studied despite its relevance concerning the demonstration of industrial feasibility. For achieving such high production rates, more attention must be paid to different features such as high active site density, high turnover frequency (TOF), and efficient mass transport of the chemical species from and toward the electrocatalysts to optimize the reaction overpotentials.

However, most transition metal compounds are not stable under the oxidizing conditions of OER, and the influence of the chemical transformation of these materials in the catalytic reaction should be considered.[8−11] Usually, metal (oxy)-hydroxides are generated in situ at the surface of oxides, selenides, or even phosphides.[3,9,10,12−14] In some cases, the transformation is not only limited to the surface and also affects the electrocatalyst bulk, which could be detrimental if the new material possesses low conductivity. A detailed analysis of the material conversion and the role of the non-metallic element need to be faced for a complete rational design of the anode. Metal (oxy)hydroxides are well known to have a high electrocatalytic performance, providing highly active sites for OER,[9,15−17] especially those containing Fe, Co, or Ni.[18−20] In fact, for these materials, the combination of Fe with Ni or Co has led to improved activity.[21] The enhancement of the electrochemical activity for OER in bimetallic CoFe-based electrocatalysts compared with the corresponding monometallic compounds has also been corroborated by observing a decrease in the overpotentials.[9,22−24] This is a critical aspect in the design of the anodes for achieving commercially viable electrolyzers for fuel production.

In this work, we report on a detailed investigation of CoFe bimetallic phosphide and the transformation mechanism in alkaline electrolyte leading to high-performance anodes for OER at high current densities, >1 A cm^{-2}. The rational procedure to prepare the electrodes involves as the first step the synthesis of tiny nanorods mainly composed of CoFeP. They are obtained by a "heating up" process using triphenyl phosphite (TPOP) which is advantageous against other phosphorous precursors because it is air-stable and inexpensive.[25] A nickel foam (NF) substrate has been selected as a 3D scaffold of the electroactive material because of its high conductivity and porous structure. The simplicity of the method employed for loading the electrocatalyst should be highlighted because of its potential scalability and the fact that no additives or heat treatments are used. The CoFeP/NF electrodes were characterized from a morphological, structural, physicochemical, and functional point of view before and after OER in alkaline electrolyte. The most significant results concern the depletion of phosphorus (linked to the formation of CoFe oxyhydroxide) and the radically different morphology between the initial nanorod-like shape found in the CoFeP powder and the nanoplate-like shape of the oxyhydroxide after OER. All of these characteristics allow a rational design of the anode for working at high current densities. Then, the effectivity of the proposed strategy for the anode design is tested for reaching 1 A cm^{-2} for OER. The significance of the transformation of the bimetallic phosphide into a bimetal oxyhydroxide and the role played by phosphorus have been analyzed.

EXPERIMENTAL SECTION

Synthesis of Colloidal CoFeP Nanoparticles. For the synthesis of the CoFeP nanoparticles,[26] 2.4 g (10 mmol) of 1-hexadecylamine (HDA, 90%, Acros Organics) was mixed with 10.0 mL of 1-octadecene (ODE, 90%, ACROS Organics) and 2.6 mL (10 mmol) of TPOP (99%, ACROS Organics) in a 50 mL flask. The system was degassed, heated to 130 °C, and kept at this temperature for 1 h to remove low boiling point impurities, moisture, and oxygen. Then, the mixture was cooled down to 60 °C, and 4 mL of ODE containing 380 mg (1 mmol) $Co_2(CO)_8$ (95%, ACROS Organics) and 0.3 mL of (2 mmol) $Fe(CO)_5$ (Sigma-Aldrich) were added. First, the temperature was increased to 230 °C, and then, the mixture was stirred for 30 min. Second, the mixture was heated to 300 °C for 40 min and kept at this temperature for 1 h. Finally, the system was allowed to cool down to 200 °C by removing the heating mantle and subsequently cooled rapidly down to room temperature with a water bath. The product was precipitated using acetone and centrifuged for 3 min at 7500 rpm. To remove organics, three dispersion and precipitation cycles using chloroform and acetone were additionally carried out to obtain a cleaner CoFeP precipitate. To synthesize the Co_2P nanoparticles used as the reference material, an identical procedure was followed but without adding the iron precursor.

Ligand Removal. 10 mL of a dispersion CoFeP or Co_2P in hexane (10 mg mL^{-1}) was mixed with 10 mL of acetonitrile to form a two-phase mixture. Afterward, 1 mL of HBF_4 solution (48%) was added. The resulting solution was sonicated until the nanoparticles transferred from the upper to the bottom layer. Finally, these nanoparticles were washed with ethanol three times and dispersed in 10 mL of ethanol with around 0.5 mL of *N*,*N*-dimethylformamide for further use.

Electrode Preparation. NF substrates were cleaned in an ultrasonic bath in 1 M HCl, water, and ethanol for 10 min in each one. A suspension of 10 mg mL^{-1} of the CoFeP nanoparticles in ethanol was sonicated for 30 min. The cleaned NF substrates were dipped into this suspension for 30 s, and subsequently, the excess dispersion was removed. Finally, the electrode was dried at ambient temperature. The deposited amount of catalyst used for the objective of this work was estimated to be enough to guarantee enough active site density > 10^{18} cm^{-2} to facilitate reaching a current density higher than 1 A cm^{-2}. Electrodes with a higher amount of electrocatalyst have been prepared by repeating the immersion and drying steps up to four times. Unless otherwise stated, the electrodes were prepared with a single immersion, and the samples named "after OER" were previously subjected to a current density of ca. 120 mA cm^{-2} for 2 h.

Morphological, Structural, and Physicochemical Characterization. Structural characterization was performed by X-ray diffraction (XRD) using a Bruker D8 Advance diffractometer equipped with a Cu Kα (1.5406 Å) radiation source, LYNXEYE super speed detector, and Ni filter. A Bragg−Brentano (θ−2θ) configuration was used with a step size of 0.025°. The morphology of the electrodes was analyzed by a Zeiss Auriga 60 field emission scanning electron microscope (FESEM). Both the high-resolution transmission electron microscopy (HRTEM) and scanning transmission electron microscopy (STEM)−electron energy-loss spectroscopy (EELS) are obtained in an FEI F20 at 200 kV. The HRTEM was acquired with a condenser aperture of 100 μm, no objective aperture, spot size 3, and a BM-UltraScan CCD camera. The STEM−EELS was acquired with a condenser aperture of 70 μm, no objective aperture, nominal camera length 30 mm, spot size 6, and Gatan EF-CCD camera. The same conditions apply for STEM−energy dispersive X-ray (EDX), with a detector EDAX super ultra-thin window X-ray detector, 136 eV resolution (Z > Z(Be)), and a detector area of 30 mm^2. The EELS and EDX supporting STEM images are obtained using an annular dark field detector (DF4). For analyzing the samples, the initial CoFeP or Co_2P samples were diluted in hexane before deposition on the grid. For the analysis of the electrode after OER, the electrocatalyst was scraped from the NF substrate, and the resulting powder was dispersed in hexane by sonication before the deposition on the grid. For the X-ray photoelectron spectroscopy

https://doi.org/10.1021/acsaem.3c00032
ACS Appl. Energy Mater. 2023, 6, 5690−5699

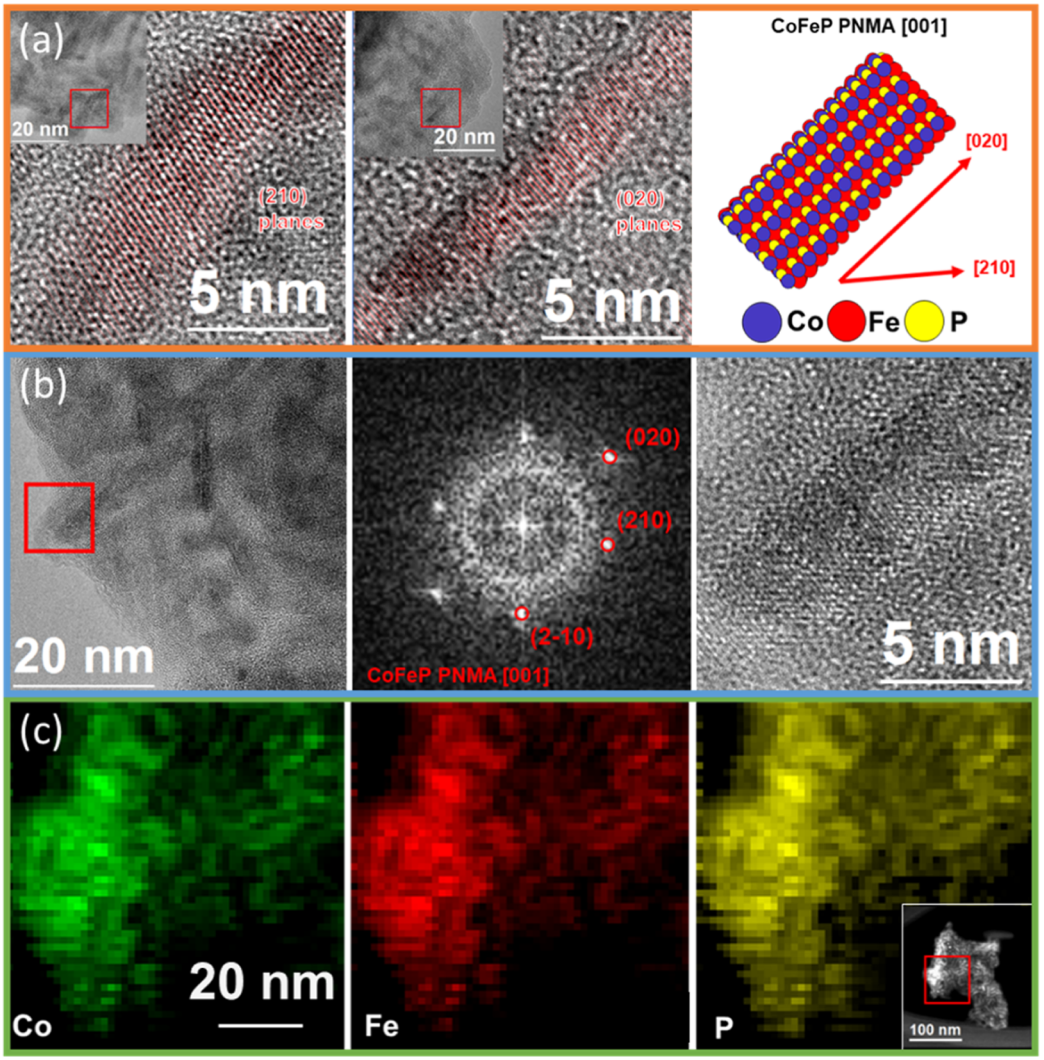

Figure 1. (a) HRTEM images showing individual nanorods (from the red squared region in the lower magnification images in the inset) and the schematic illustration of the orientation of the nanorods on the right side. (b) FFT spectrum corresponding to the HRTEM image of a CoFeP nanorod on the right that corresponds to the red squared region of the image on the left. (c) EELS compositional maps of Co, Fe, and P in CoFeP nanorods. The inset shows the corresponding STEM-ADF image.

(XPS) analysis, a monochromatic X-ray source Al Kα line was used in both a PHI 5500 Multitechnique System (Physical Electronics) for the electrodes before OER and a NEXSA X-ray photoelectron spectrometer (Thermo-Scientific) for the electrodes after OER.

Electrochemical Measurements. The electrochemical performance of the CoFeP-based electrodes was analyzed with a Biologic VMP-300 potentiostat using a three-electrode cell. All the potentials were measured against an Ag/AgCl reference electrode. The potentials in the RHE scale are calculated according to E(vs RHE) = E(vs Ag/AgCl) + 0.205 V + 0.059·pH. To evaluate the OER activity, linear sweep and cyclic voltammetries were performed at a scan rate of 5 mV s^{-1} in 1 M KOH. All the potentials were corrected with the IR drop, and the corresponding resistance (R) was determined by electrochemical impedance spectroscopy (EIS). The overpotentials were calculated in all cases as $\eta = E - 1.23$ V, where E is the applied potential vs RHE. The determination of double-layer capacitance (C_{dl}) by cyclic voltammetries was performed between 0.1 and 0.2 V vs Ag/AgCl, a potential region with no faradaic processes, at different scan rates. The electrochemically active surface area (ECSA) was calculated as C_{dl}/C_s, where C_s is a reference capacitance for a planar surface taken as 40 μF cm^{-2}.[27,28] Nyquist plots were obtained by EIS in the frequency range of 50 kHz to 100 mHz and employing a signal amplitude of 10 mV. The fitting of the experimental EIS curves to the equivalent circuit was performed with the Biologic software. The calculation of the TOF can differ from study to study.[27] In this work, TOF is calculated as the number of product molecules (O_2) per second and active site: TOF = $jA/(4Ne)$, where j is the current density, A is the area, N is the number of active sites, and e is the elementary charge constant (1.6×10^{-19} C). The calculated number of active sites is 3.2×10^{18} and 2.3×10^{18} for CoFeP and Co_2P, respectively. They are estimated considering that both Co and Fe metallic atoms act as active sites. The metallic content was calculated by the difference of the electrode mass after and before the electrocatalyst loading and the elemental ratios obtained by EDX in the as-prepared electrodes. In the full cell assembly, water splitting was performed in a two-electrode configuration with the two compartments separated by a Sustainion (Dioxide Materials) alkaline exchange membrane. The gas outlets from the anodic and cathodic compartments were connected to two inverted graduated cylinders filled with water to measure accumulated O_2 and H_2, respectively. For the theoretical calculation of the volumes, they are considered ideal gases. The presence of H_2 was corroborated by gas chromatography using He as a carrier gas.

RESULTS AND DISCUSSION

Characterization of the CoFeP Nanoparticles and the Fabricated CoFeP/NF Electrode. The bimetallic CoFeP

https://doi.org/10.1021/acsaem.3c00032
ACS Appl. Energy Mater. 2023, 6, 5690−5699

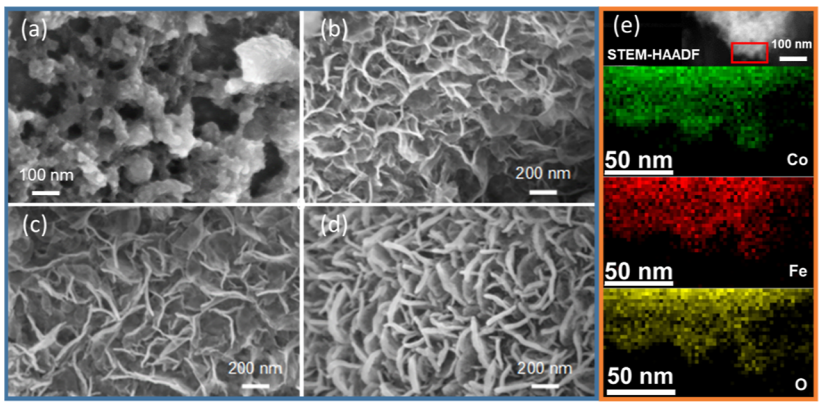

Figure 2. SEM micrographs showing the morphology of the (a) as-prepared and after (b) 5, (c) 30, and (d) 120 min of OER for a CoFeP/NF electrode. (e) EELS compositional maps of the powder obtained by scraping the electrocatalyst from the electrode surface of the CoFeP/NF electrode after 120 min of OER.

nanoparticles obtained by the TPOP route were characterized in terms of morphology, crystallinity, and composition. HRTEM images were recorded to obtain information about the nanostructure morphology. Figures 1a,b and S1 show the synthesized CoFeP nanoparticles exhibiting a nanorod-like shape with a length up to about 18 nm and a diameter of 2−4 nm. FFT (fast Fourier transform) in Figure 1b reveals the presence of the CoFeP PNMA 62 phase that is according to the XRD analysis in Figure S2. Importantly, the planes observed in isolated nanorods (Figure 1a) can be ascribed to the (020) and (210) planes of CoFeP PNMA. Figure 1a shows a sketch of the nanorod crystallographic arrangement. It was observed that these rods present a growth direction [010] (and its corresponding (020) observed planes), which coincides with the longitudinal axis of the nanorods, which is further supported by its relative orientation with the resolved (210) planes of CoFeP. Additionally, EELS compositional maps of Co, Fe, and P were also performed to get insights into the nanostructure composition. Figure 1c shows a particle composed of the coalescence of different nanorods. A similar spatial distribution of the three elements along all the particles was found, coherent with the expected stoichiometry of the CoFeP. Nevertheless, EELS quantification reveals a slightly higher concentration of Co against Fe, Co/Fe ≈ 1.5. Monometallic Co_2P nanoparticles were also analyzed by HRTEM. They also exhibit rod-like shapes (Figure S3), having similar sizes to the bimetallic nanorods. The planes found have similar interplanar distances to that of CoFeP and are according to the Co_2P PNMA, which was further corroborated by FFT (Figure S4). As in the case of CoFeP, Co and P are homogeneously distributed through the Co_2P nanorods as revealed by EELS (Figure S5). In both CoFeP and Co_2P nanoparticles, the metal to phosphorous ratio, based on the atomic concentration obtained by EDX, was near 1.3, which is lower than the stoichiometric. This can be partly due to the presence of oxygenated species such as metal phosphates or the presence of CoP as a secondary phase.

XPS is used to gather information about the first fourth or sixth atomic monolayers (2−3 nm) at the sample surface. This has been employed to characterize the surface composition and chemical nature of the synthesized electrocatalyst, although it can be altered by the interaction with the ambient air after its deposition on the NF. The full survey spectrum of a bare CoFeP/NF electrode shown in Figure S6 reveals the presence of Co, Fe, P, O, and C. In the P 2p spectra (Figure S7), the largest peak is located near 133.3 eV and can be correlated with the presence of phosphate species.[9,10] This confirms that the surface of the electrocatalyst is composed of a metal phosphate rather than a phosphide after air exposure, which usually occurs in metal phosphides.[15,23] The Co 2p spectrum in Figure S7 exhibits the $2p_{3/2}$ and $2p_{1/2}$ signals with the overlapping of different contributions including satellite peaks. The fact that the position of the strongest peak in the Co $2p_{3/2}$ region (781.2 eV) was higher than the typical peak positions of metal oxides, together with the predominant peak in the O 1s region at 531.1 eV (Figure S7), is in agreement with the presence of metal phosphate.[29,30] The small peak located at 778.1 eV in Co $2p_{3/2}$ could be assigned according to some authors to the presence of metal phosphides, although the corresponding Co $2p_{1/2}$ signal is challenging to be identified probably because of the small amount of phosphide detected at the surface.[9,24] Accordingly, a very small peak at 130.1 eV in the P 2p spectrum can be attributed to metal phosphide. The Fe $2p_{3/2}$ signal (Figure S7) revealed the presence of oxidized iron species.[9] Therefore, the results from the XPS characterization indicate that the outer layer of the electrocatalyst surface shows a transformation from metal phosphide to phosphate, even when the samples were stored in a protective atmosphere before the analysis.

Characterization of the CoFeP-Based Electrodes as Anodes for OER. Metal phosphides can be unstable in alkaline media (1 M KOH) under anodic conditions, and then a detailed physicochemical characterization was performed before and after OER to study the material transformation and especially the role of phosphorous. Despite the transformation, the electrodes were stable for OER, and any significant decay of the current was observed at about 100 mA cm^{-2} (Figure S8). Figure 2a−d shows the morphology of the CoFeP nanostructures on the NF surface before and after OER by FESEM images. The small particle size of the CoFeP nanorods favors a good dispersion of the electrocatalyst on the NF surface. In the as-prepared electrodes, a porous network of interconnected nanoparticles with spherical shape is observed (Figure 2a), probably derived from the coalescence of the initial CoFeP nanorods observed in Figure 1a and the oxidation of the surface leading to an outer metal phosphate layer. The CoFeP/NF electrodes were analyzed after chronoamperometries at different times selecting a potential in the OER region with a current density near 100 mA cm^{-2}. A radical change of the overall morphology was observed (Figure

https://doi.org/10.1021/acsaem.3c00032
ACS Appl. Energy Mater. 2023, 6, 5690−5699

2b−d) after OER, now displaying nanostructures with a plate-like shape resembling 2D units and thus conferring high effective area to the electrode. However, there was no significant evolution of the morphology from 5 to 120 min of OER. The approximate dimensions of the nanoplates are 200−400 and 10−40 nm in length and thickness, respectively. For comparison purposes, the Co_2P/NF electrodes were also analyzed by SEM before and after OER (Figure S9). A similar morphological change was observed after 120 min of OER, although in this case, the nanoplates were smaller with an approximate length of 60 nm and a thickness of 10 nm.

Despite the huge transformation of the material, a homogeneous distribution of Co and Fe is observed in the EELS maps as shown in Figure 2e. Remarkably, we could not observe any presence of crystalline planes in the HRTEM images neither in the corresponding FFT patterns obtained in the samples after OER, pointing out the amorphous nature of the transformed material. Furthermore, the high oxygen signal together with the absence of phosphorous suggests that oxygenated phases as oxygen and hydroxyl groups have replaced the initial phosphide/phosphate species forming oxyhydroxide structures. To further investigate these assumptions, high-resolution XPS spectra shown in Figures 3 and S10

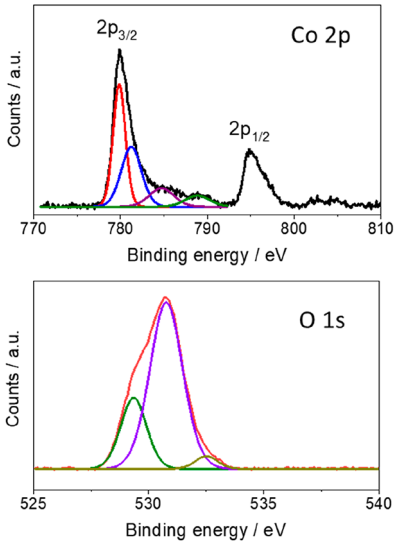

Figure 3. XPS spectra in the Co 2p and O 1s regions for the CoFeP/NF electrodes after OER.

in the electrodes after OER are compared with the previous results using fresh samples (Figure S7). To increase the intensity of the XPS signal, the analysis was performed in a sample synthesized by four immersions in the iron precursor dispersion. We must stand out on several significant features. On one hand, there is a low concentration of residual phosphorous at the surface (see Table S1). On the other hand, a significant change in the O 1s spectrum is noticeable after OER (Figure 3). Apart from the peak around 532.5 eV that can be attributed to absorbed H_2O, the main signal can be deconvoluted into two peaks. The one at 529.4 eV is according to M−O and the largest peak at 530.8 eV would correspond to M−OH species supporting the presence of metal oxyhydroxides.[15] These characteristics are endorsed for the measured spectra of Co 2p and Fe 2p shown in Figures 3, S7, and S10, in which the most intense peaks in the $2p_{3/2}$ signals are shifted to lower energies in agreement with the expected values of oxyhydroxides compared to the initial phosphates. Therefore, after the electrochemical measurements in alkaline media, the material is transformed in terms of morphology and composition from the initial CoFeP to $CoFeO_xH_y$. After immersing in the 1 M KOH solution, a morphological change occurs; afterward, the cyclic voltammogram of the CoFeP (Figure S11) shows an anodic irreversible peak appearing at 1.35 V vs RHE that is only present in the first cycle. This peak has been attributed to the irreversible evolution of CoOOH.[19,31,32] Accordingly, a peak near the same potential region was also observed in the Co_2P/NF electrodes. After this anodic peak, the current densities for OER remain constant, as evidenced by the overlapping of the first and second voltammetric curves shown in Figure S11. The complete morphological transformation of the CoFeP structure together with the phosphorous loss leading to $CoFeO_xH_y$ is favored by the small size of the initial nanoparticles and the interconnected porous network formed by these nanoparticles that facilitate the permeability of the alkaline electrolyte. Raman analysis shown in Figure S12 supports the presence of metal oxyhydroxide. Concretely, the bands at 575 and 675 cm^{-1} can be correlated with cobalt and iron oxyhydroxides,[33−35] although the presence of oxides/hydroxides as secondary phases cannot be discarded. On the other hand, Co_2P/NF electrodes were also analyzed by XPS after OER (Figure S13). No differences in the oxidation states of cobalt with respect to the bimetallic material are observed, as the Co 2p region presents the same characteristics.

Electrochemical Analysis of the Electrodes Fabricated Using CoFeP as the Electrocatalyst. The electrochemical activity of the initial bimetallic CoFeP/NF transformed to $CoFeO_xH_y$/NF has been investigated in a 1 M KOH electrolyte. Figure 4a shows the cyclic voltammograms after IR correction for the CoFeP/NF electrode, compared with both the Co_2P/NF electrode and the bare NF scaffold. The bimetallic CoFeP/NF electrode presents the best catalytic activity for OER, outperforming the monometallic Co_2P/NF. The overpotentials for OER at 10 and 100 mA cm^{-2} are 285 and 335 mV for CoFeP/NF and 345 and 410 mV for Co_2P/NF, respectively. The bare NF also presents electrochemical activity for OER in alkaline media[36−38] but significantly lower than the bimetallic phosphide-loaded electrodes. The Tafel representation depicted in Figure 4b further confirms the favorable OER kinetics in the bimetallic electrocatalyst. The Tafel slope for Co_2P/NF is 53 mV dec^{-1}, while for CoFeP/NF, it is as low as 42 mV dec^{-1}. To the best of our knowledge, the latter value is the lowest reported for cobalt iron phosphide-based anodes without using a hybrid material (as compared in Table S2). Additionally, the behavior of the CoFeP/NF electrodes was tested during cycling for OER displaying good stability after 500 cycles (Figure S14).

Electrodes with different deposited amount of electrocatalysts were prepared by repeating different cycles of immersion in the CoFeP dispersion and drying up to four times, leading to different catalyst loading (see the inset of Figure S15a). The applied potentials for a given current density are reduced as the catalyst loading increases as expected. For 10 mA cm^{-2}, the overpotential is 270 mV for four immersions, 15 mV lower than for the one of a single immersion (Figure S15a). However, as the catalyst loading increases, the current density normalized by the mass loading decreases (Figure S15b). Then, for the lowest loaded amount of catalyst, there is an optimum dispersion of the CoFeP on

https://doi.org/10.1021/acsaem.3c00032
ACS Appl. Energy Mater. 2023, 6, 5690−5699

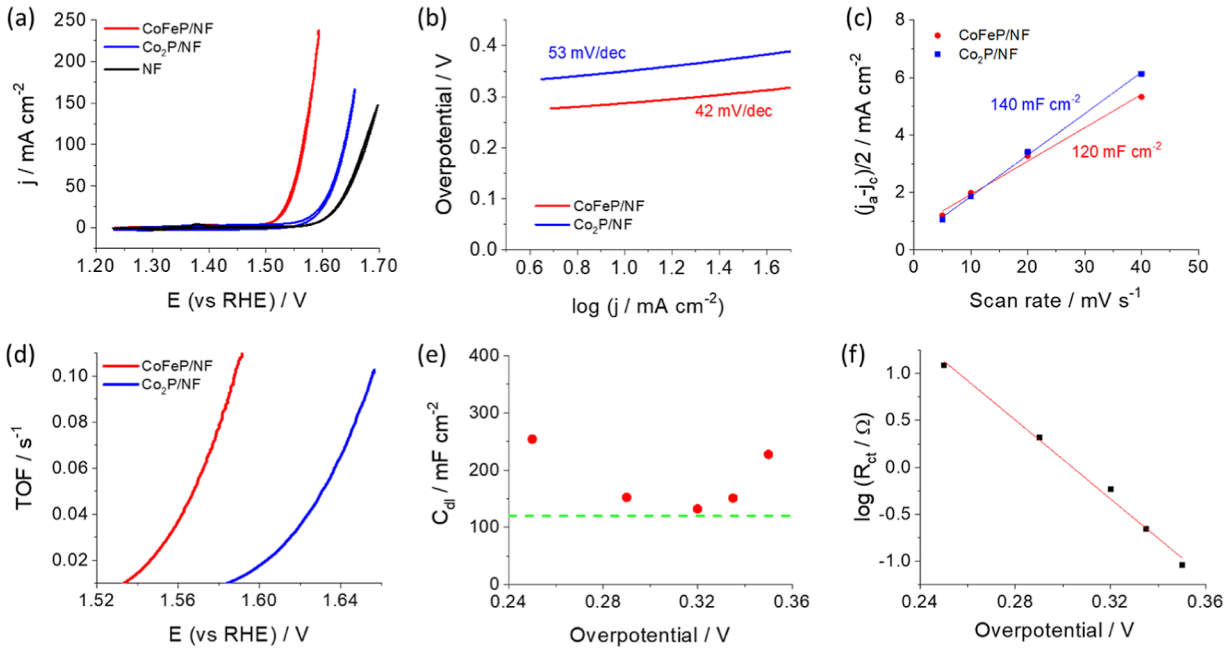

Figure 4. (a) Cyclic voltammogram recorded at 5 mV s^{-1}, (b) Tafel plots, (c) $(j_a - j_c)/2$ vs scan rate plot, and (d) calculated TOF values as a function of the potential for CoFeP/NF and Co_2P/NF in 1 M KOH. (e) C_{dl} and (f) log (R_{ct}/Ω) vs overpotential from the Nyquist plots for CoFeP/NF in 1 M KOH. The green line in (e) indicates the C_{dl} value obtained from cyclic voltammograms in (c) and the red line in (f) the linear fitting.

the NF maximizing the number of reactive sites available per overall amount of catalyst. The overpotentials achieved in this work, considering the loaded amount of electrocatalyst, are one of the lowest reported for CoFeP-based anodes for OER (see Table S2).

To get more insights into the origin of the catalytic activity of $CoFeO_xH_y$ obtained from the bimetallic phosphide, the double-layer capacitances were calculated from $(j_a - j_c)/2$ vs the scan rate plot obtained from Figure S16. The calculated C_{dl} values are similar for the CoFeP/NF and Co_2P/NF and are estimated as 120 and 140 mF cm^{-2}, respectively, as shown in Figure 4c. Then, the ECSA values of 3000 and 3500 cm^2 are obtained for CoFeP/NF and Co_2P/NF, respectively, referred to a planar surface. The huge ECSA values can be correlated with a high density of active sites due to good dispersion of the material favored by its low particle size and the porous structure of the electrode scaffold that allow the full penetration of the electrolyte.

Figure 4d displays TOF values deduced from the calculated number of active sites based on the loaded amounts of electrocatalysts. A TOF value of 0.1 s^{-1} is reached at 358 mV for the CoFeP/NF, while for Co_2P/NF, 425 mV is required. This demonstrates that despite both electrodes possessing similar ECSA and estimated number of active sites, the bimetallic phosphide exhibits a faster kinetic toward OER. This may be caused by the catalytic effects of the metallic Co and Fe adjacent sites cooperating on the four steps of the water oxidation reaction. This is supported by the lower value of Tafel slope in the CoFeP/NF electrode. In this regard, some decrease in the concentration of iron in the fabricated CoFeP nanoparticles is not critical in the OER activity, as when it decreases by 40%, the bimetallic electrode produces similar overpotentials. This is in agreement with a previous work using comparable Co/Fe ratios.[15] A contribution derived from the nickel substrate cannot be discarded as active nickel species for OER can be generated in the alkaline electrolyte.

Nyquist plots obtained from EIS are useful to better understand the electrocatalyst kinetics for OER. Then, they were recorded at different applied potentials (Figure S17a), and the obtained spectra were fitted according to the model circuit displayed in Figure S17b. R_Ω is the electrolyte resistance and the R_I and Q_I (a constant phase element) at high frequencies can be tentatively associated with the Ni/electrocatalyst interface or to the presence of a passive film.[39] C_{dl} and R_{ct} are related to the charge transfer to the electrolyte, and they can provide information about the OER kinetic parameters. Concretely, the exchange current density (j_0) and the Tafel slope (b) can be estimated from the Nyquist plots using the following expression[40−42]

$$\log\left(\frac{1}{R_{ct}}\right) = \log\left(\frac{di}{d\eta}\right) = \frac{1}{b}\eta + \log\left(\frac{2.3j_0}{b}\right) \quad (1)$$

where $b = 2.3RT/\alpha_a F$ in mV dec^{-1}, being α_a the overall transfer coefficient given by $\alpha_a = (n_f/\nu + n_r\beta_a)$, where n_f is the number of electrons transferred before the rate-determining step (rds), ν is the stoichiometric number with a typical value of one, n_r is the number of electrons transferred in each occurrence of the rds, and β_a is correlated with the symmetry factor.[43,44] On one hand, C_{dl} values calculated from Figure S17 are represented in Figure 4e as a function of the overpotential. Although they are in the same order of magnitude as that obtained by cyclic voltammograms in the region without faradaic currents (Figure 4c), there exist some dispersion of the values in the considered range of potentials. On the other hand, according to eq 1, Figure 4f shows a linear relationship between log(R_{ct}) and η. The points in Figure 4f can be fitted to a straight line with good fitting (R^2 = 0.996). The Tafel slope (b) can be calculated as 48 mV dec^{-1}, while a value of 42 mV dec^{-1} was determined from the voltammogram shown in Figure 4b.

https://doi.org/10.1021/acsaem.3c00032
ACS Appl. Energy Mater. 2023, 6, 5690−5699

Then, the overall charge transfer coefficient (α_a) can be calculated as 1.24−1.41. Such values suggest that a step subsequent to the first electron transfer is the rds with $\nu = 1$, $n_f = 1$ and $n_r = 1$.[44] According to eq 1, from the intercept with the y-axis, the exchange current density is calculated to be 1.1×10^{-5} mA cm^{-2}.

The excellent characteristics based on the kinetics and the active site density suggest that the synthesized CoFe-based anodes are good candidates for working at high current densities as feasible and reliable electrodes. Thus, the electrochemical activity of these anodes was evaluated at higher applied potentials, and the effect of the temperature was studied. Figure 5a shows the potential region of current

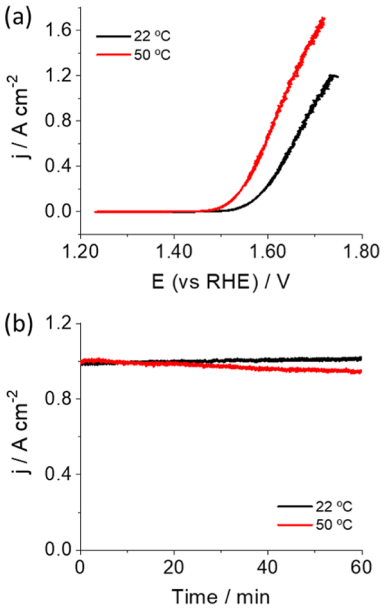

Figure 5. (a) Cyclic voltammogram and (b) chronoamperogram at a current density of ca. 1 A cm^{-2} at 22 and 50 °C for the CoFeP/NF electrode in 1 M KOH.

densities >1 A cm^{-2} at 22 and 50 °C. For reaching 1 A cm^{-2}, the overpotential is only 475 mV, and they decrease by 70 mV when the temperature rises to 50 °C. Furthermore, the stability tests at 1 A cm^{-2} in Figure 5b show that the current density remains constant at 22 °C, while at 50 °C, there is a slight decrease with time, which may be due to a lack of thermal stability of the experimental setup. Table 1 summarizes the approximate overpotential values achieved for 10, 100, and 1000 mA cm^{-2} based on Figure 5a.

Anion Exchange Membrane Water Electrolysis Performance. The stability of the electrocatalysts is a critical issue in fuel production and should be tested under more realistic conditions of continuous electrolyte flow to better evaluate its commercial viability. For this goal, the developed

Table 1. Overpotentials for OER at Selected Current Density Values at 22 and 50 °C

	η/mV	
j/mA cm^{-2}	22 °C	50 °C
10	285	240
100	335	290
1000	475	405

cobalt iron oxyhydroxide anode was integrated into an electrolyzer schematized in Figure 6a for H_2 and O_2

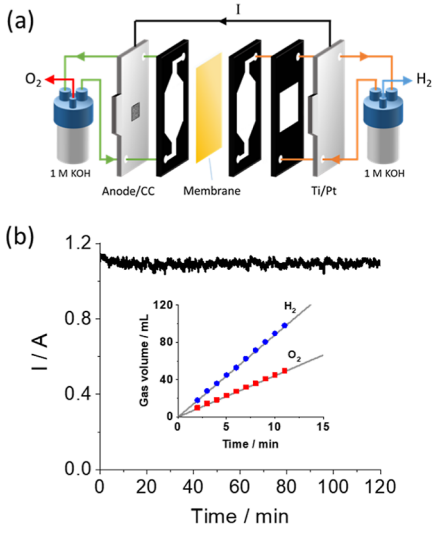

Figure 6. (a) Sketch of the alkaline exchange membrane electrolyzer using geometric electrodic areas of 1 cm^2 in the anode and 10 cm^2 for the Ti/Pt cathode. CC = current collector. (b) Chronoamperogram in the full cell depicted in (a) at a current density near 1 A and heating the electrolytes to 50 °C. Inset: experimental (points) and calculated (solid lines) accumulated volumes of H_2 and O_2.

production, which is a relevant configuration for an industrial application. The cell comprises two compartments separated by an alkaline anion membrane, with the anolyte and catholyte recirculating at a high flow rate through the respective compartments. Consequently, this configuration allows for the separation and collection of both produced gases, where hydrogen evolves in the Ti/Pt plate (10 cm^2) and oxygen evolves in the $CoFeO_xH_y$/NF anode with a geometric area of 1 cm^2.

The stability of the full cell was examined at a high current density of nearly 1 A by heating the electrolytes at 50 °C. Figure 6b shows good stability of the current during 2 h, without any significant decay. Additionally, the volumes of H_2 and O_2 were measured for 10 min after 2 h at 1 A in the same conditions. The inset of Figure 6b displays the points corresponding to the measured gas volumes, while the straight lines correspond to the calculated values. An excellent agreement between the experimental and theoretical values was found, which means that the faradaic efficiency for OER and HER in both processes is near 100%. The outlet gas stream from the cathode was analyzed by gas chromatography confirming the presence of hydrogen gas. Similar results were obtained at room temperature (Figure S18) displaying also good stability. In that case, because of the lack of temperature control, an initial increase in the current was observed before thermal equilibration.

CONCLUSIONS

In this work, an efficient anode for OER obtained by the in situ generation of amorphous cobalt iron oxyhydroxide from the corresponding bimetallic phosphide on NF is reported. In the chemical conversion, phosphorous acts as a sacrificial element for homogeneous metal oxyhydroxide formation facilitated by the electrolyte permeation within the nanoporous structure. The initial CoFeP/NF electrode is synthesized from tiny rod-

https://doi.org/10.1021/acsaem.3c00032
ACS Appl. Energy Mater. 2023, 6, 5690−5699

like nanoparticles of bimetallic phosphide obtained by a feasible and scalable synthesis. These nanorods were dispersed in a 3D framework of a highly conductive nickel foam as a key element in the anode design. It ensures a high density of active sites as well as an appropriate pore size to guarantee the release of oxygen gas. Under alkaline media and anodic polarization, apart from the phosphorous depletion, the morphology radically changes from the initial nanorods to CoFe-oxyhydroxide nanoplates with a high ECSA. Remarkably, this procedure guarantees maintaining a homogeneous distribution of metal atoms on the nickel foam that allows for a rational design of the anodes to achieve a high density of active sites. The presence of Co and Fe atoms promotes favorable catalytic effects on the four-step reaction of water oxidation. Then, this rational anode design allows achieving working conditions of high current densities (higher than 1 A cm^{-2}) at optimized overpotentials lower than 500 mV for 1 A and Tafel slope as low as 42 mV dec^{-1}. Remarkably, apart from the feasible and scalable manufacturing route of the $CoFeO_xH_y$/NF electrode, its stability was excellent in an alkaline exchange membrane flow cell at 1 A, which makes this electrode a robust and promising anode in high production rate devices for fuel electrosynthesis.

■ ASSOCIATED CONTENT

Supporting Information

The Supporting Information is available free of charge at https://pubs.acs.org/doi/10.1021/acsaem.3c00032.

Supplementary HRTEM images, XRD pattern, EELS compositional maps, XPS spectra, chronoamperograms (stability tests), SEM images, atomic percentages determined by XPS, consecutive cyclic voltammograms (CVs) (stability test), CVs for different loading amounts of electrocatalyst, CVs at different scan rates for ECSA determination, Raman spectrum, Nyquist plots, volumes of H_2 and O_2 generated in full cell and table for the comparison of CoFeP-based electrodes (PDF)

■ AUTHOR INFORMATION

Corresponding Author

María Isabel Díez-García − *Catalonia Institute for Energy Research (IREC), 08930 Barcelona, Spain;* orcid.org/0000-0001-9939-8642; Email: midiez@irec.cat

Authors

Guillem Montaña-Mora − *Catalonia Institute for Energy Research (IREC), 08930 Barcelona, Spain*

Marc Botifoll − *Catalan Institute of Nanoscience and Nanotechnology (ICN2), CSIC and BIST, Barcelona, Catalonia 08193, Spain*

Andreu Cabot − *Catalonia Institute for Energy Research (IREC), 08930 Barcelona, Spain; ICREA, Barcelona, Catalonia 08010, Spain;* orcid.org/0000-0002-7533-3251

Jordi Arbiol − *Catalan Institute of Nanoscience and Nanotechnology (ICN2), CSIC and BIST, Barcelona, Catalonia 08193, Spain; ICREA, Barcelona, Catalonia 08010, Spain;* orcid.org/0000-0002-0695-1726

Mohammad Qamar − *Interdisciplinary Research Center for Hydrogen and Energy Storage, King Fahd University of Petroleum and Minerals, 31261 Dhahran, Saudi Arabia;* orcid.org/0000-0002-5351-9872

Joan Ramon Morante − *Catalonia Institute for Energy Research (IREC), 08930 Barcelona, Spain*

Complete contact information is available at: https://pubs.acs.org/10.1021/acsaem.3c00032

Notes

The authors declare no competing financial interest.

■ ACKNOWLEDGMENTS

The project on which these results are based has received funding from the European Union's Horizon 2020 research and innovation programme under Marie Skłodowska-Curie grant agreement no. 801342 (Tecniospring INDUSTRY) and the Government of Catalonia's Agency for Business Competitiveness (ACCIÓ). The authors extend their overall appreciation to the Deputyship for Research & Innovation, Ministry of Education in Saudi Arabia for funding this research work through the project number DRI 598. M.I.D.-G. acknowledges the support from Ministerio de Ciencia e Innovación in Spain through the Juan de la Cierva fellowship (FJC2018-036229-I). M.I.D.-G. acknowledges M. Biset-Peiró (IREC) and S. Murcia (IREC) for their help in this work. M.B. acknowledges funding from the Catalan Agency for Management of University and Research Grants (AGAUR) Generalitat de Catalunya formation of investigators (FI) PhD grant. ICN2 and IREC receive support from the CERCA Programme/Generalitat de Catalunya and program 2021 SGR 00457 and 2021 SGR 01581. The authors thank support from the projects NANOGEN (PID2020-116093RB-C43) and CERES (PID2020-116093RB-C42), funded by MCIN/AEI/10.13039/501100011033/. ICN2 is supported by the Severo Ochoa program from Spanish MCIN / AEI (Grant No.: CEX2021-001214-S).

■ REFERENCES

(1) Li, Y.; Dong, Z.; Jiao, L. Multifunctional Transition Metal-Based Phosphides in Energy-Related Electrocatalysis. *Adv. Energy Mater.* **2020**, *10*, 1902104.

(2) Zhang, T.; Han, X.; Liu, H.; Biset-Peiró, M.; Zhang, X.; Tan, P.; Tang, P.; Yang, B.; Zheng, L.; Morante, J. R.; Arbiol, J. Quasi-Double-Star Nickel and Iron Active Sites for High-Efficiency Carbon Dioxide Electroreduction. *Energy Environ. Sci.* **2021**, *14*, 4847−4857.

(3) Jin, Z.; Li, P.; Xiao, D. Metallic Co_2P Ultrathin Nanowires Distinguished from CoP as Robust Electrocatalysts for Overall Water-Splitting. *Green Chem.* **2016**, *18*, 1459−1464.

(4) Xiao, P.; Chen, W.; Wang, X. A Review of Phosphide-Based Materials for Electrocatalytic Hydrogen Evolution. *Adv. Energy Mater.* **2015**, *5*, 1500985.

(5) Pei, Y.; Cheng, Y.; Chen, J.; Smith, W.; Dong, P.; Ajayan, P. M.; Ye, M.; Shen, J. Recent Developments of Transition Metal Phosphides as Catalysts in the Energy Conversion Field. *J. Mater. Chem.* **2018**, *6*, 23220−23243.

(6) Xu, S.; Zhao, H.; Li, T.; Liang, J.; Lu, S.; Chen, G.; Gao, S.; Asiri, A. M.; Wu, Q.; Sun, X. Iron-Based Phosphides as Electrocatalysts for the Hydrogen Evolution Reaction: Recent Advances and Future Prospects. *J. Mater. Chem. A* **2020**, *8*, 19729−19745.

(7) Dutta, A.; Pradhan, N. Developments of Metal Phosphides as Efficient OER Precatalysts. *J. Phys. Chem. Lett.* **2017**, *8*, 144−152.

(8) Zhang, H.; Maijenburg, A. W.; Li, X.; Schweizer, S. L.; Wehrspohn, R. B. Bifunctional Heterostructured Transition Metal Phosphides for Efficient Electrochemical Water Splitting. *Adv. Funct. Mater.* **2020**, *30*, 2003261.

(9) Liu, X.; Yao, Y.; Zhang, H.; Pan, L.; Shi, C.; Zhang, X.; Huang, Z. F.; Zou, J. In Situ-Grown Cobalt−Iron Phosphide-Based Integrated Electrode for Long-Term Water Splitting under a Large Current

Density at the Industrial Electrolysis Temperature. *ACS Sustain. Chem. Eng.* **2020**, *8*, 17828−17838.
(10) Peng, Z.; Qiu, X.; Cai, G.; Zhang, X.; Dong, Z. Simultaneous Tuning of the Cation Content and Pore Structure of Cobalt-Iron Bimetal Phosphide to Enhance the Electrochemical Oxygen Evolution. *J. Alloys Compd.* **2020**, *842*, 155784.
(11) Wang, G. B.; Hsu, C. S.; Chen, H. M. The Individual Role of Active Sites in Bimetallic Oxygen Evolution Reaction Catalysts. *Dalton Trans.* **2020**, *49*, 17505−17510.
(12) Burke, M. S.; Enman, L. J.; Batchellor, A. S.; Zou, S.; Boettcher, S. W. Oxygen Evolution Reaction Electrocatalysis on Transition Metal Oxides and (Oxy)Hydroxides: Activity Trends and Design Principles. *Chem. Mater.* **2015**, *27*, 7549−7558.
(13) Wu, Z. P.; Lu, X. F.; Zang, S. Q.; Lou, X. W. Non-Noble-Metal-Based Electrocatalysts toward the Oxygen Evolution Reaction. *Adv. Funct. Mater.* **2020**, *30*, 1910274.
(14) Abed, J.; Ahmadi, S.; Laverdure, L.; Abdellah, A.; O'Brien, C. P.; Cole, K.; Sobrinho, P.; Sinton, D.; Higgins, D.; Mosey, N. J.; Thorpe, S. J.; Sargent, E. H. In Situ Formation of Nano Ni−Co Oxyhydroxide Enables Water Oxidation Electrocatalysts Durable at High Current Densities. *Adv. Mater.* **2021**, *33*, 2103812.
(15) Zhang, X.; Zhang, X.; Xu, H.; Wu, Z.; Wang, H.; Liang, Y. Iron-Doped Cobalt Monophosphide Nanosheet/Carbon Nanotube Hybrids as Active and Stable Electrocatalysts for Water Splitting. *Adv. Funct. Mater.* **2017**, *27*, 1606635.
(16) Wang, Y.; Kong, B.; Zhao, D.; Wang, H.; Selomulya, C. Strategies for Developing Transition Metal Phosphides as Heterogeneous Electrocatalysts for Water Splitting. *Nano Today* **2017**, *15*, 26−55.
(17) Hung, S. F.; Zhu, Y.; Tzeng, G. Q.; Chen, H. C.; Hsu, C. S.; Liao, Y. F.; Ishii, H.; Hiraoka, N.; Chen, H. M. In Situ Spatially Coherent Identification of Phosphide-Based Catalysts: Crystallographic Latching for Highly Efficient Overall Water Electrolysis. *ACS Energy Lett.* **2019**, *4*, 2813−2820.
(18) Trotochaud, L.; Young, S. L.; Ranney, J. K.; Boettcher, S. W. Nickel-Iron Oxyhydroxide Oxygen-Evolution Electrocatalysts: The Role of Intentional and Incidental Iron Incorporation. *J. Am. Chem. Soc.* **2014**, *136*, 6744−6753.
(19) Burke, M. S.; Kast, M. G.; Trotochaud, L.; Smith, A. M.; Boettcher, S. W. Cobalt-Iron (Oxy)Hydroxide Oxygen Evolution Electrocatalysts: The Role of Structure and Composition on Activity, Stability, and Mechanism. *J. Am. Chem. Soc.* **2015**, *137*, 3638−3648.
(20) Pei, Y.; Ge, Y.; Chu, H.; Smith, W.; Dong, P.; Ajayan, P. M.; Ye, M.; Shen, J. Controlled Synthesis of 3D Porous Structured Cobalt-Iron Based Nanosheets by Electrodeposition as Asymmetric Electrodes for Ultra-Efficient Water Splitting. *Appl. Catal., B* **2019**, *244*, 583−593.
(21) Chung, D. Y.; Lopes, P. P.; Farinazzo Bergamo Dias Martins, P.; He, H.; Kawaguchi, T.; Zapol, P.; You, H.; Tripkovic, D.; Strmcnik, D.; Zhu, Y.; Seifert, S.; Lee, S.; Stamenkovic, V. R.; Markovic, N. M. Dynamic Stability of Active Sites in Hydr(Oxy)-Oxides for the Oxygen Evolution Reaction. *Nat. Energy* **2020**, *5*, 222−230.
(22) Inohara, D.; Maruyama, H.; Kakihara, Y.; Kurokawa, H.; Nakayama, M. Cobalt-Doped Goethite-Type Iron Oxyhydroxide (α-FeOOH) for Highly Efficient Oxygen Evolution Catalysis. *ACS Omega* **2018**, *3*, 7840−7845.
(23) Zhang, W.; Li, Y.; Zhou, L.; Zheng, Q.; Xie, F.; Lam, K. H.; Lin, D. Ultrathin Amorphous CoFeP Nanosheets Derived from CoFe LDHs by Partial Phosphating as Excellent Bifunctional Catalysts for Overall Water Splitting. *Electrochim. Acta* **2019**, *323*, 134595.
(24) Tang, Y. J.; You, L.; Zhou, K. Enhanced Oxygen Evolution Reaction Activity of a Co_2P@NC-Fe_2P Composite Boosted by Interfaces between a N-Doped Carbon Matrix and Fe_2P Microspheres. *ACS Appl. Mater. Interfaces* **2020**, *12*, 25884−25894.
(25) Liu, J.; Meyns, M.; Zhang, T.; Arbiol, J.; Cabot, A.; Shavel, A. Triphenyl Phosphite as the Phosphorus Source for the Scalable and Cost-Effective Production of Transition Metal Phosphides. *Chem. Mater.* **2018**, *30*, 1799−1807.
(26) Zhang, C.; Du, R.; Biendicho, J. J.; Yi, M.; Xiao, K.; Yang, D.; Zhang, T.; Wang, X.; Arbiol, J.; Llorca, J.; Zhou, Y.; Morante, J. R.; Cabot, A. Tubular CoFeP@CN as a Mott−Schottky Catalyst with Multiple Adsorption Sites for Robust Lithium−Sulfur Batteries. *Adv. Energy Mater.* **2021**, *11*, 2100432.
(27) McCrory, C. C. L.; Jung, S.; Peters, J. C.; Jaramillo, T. F. Benchmarking Heterogeneous Electrocatalysts for the Oxygen Evolution Reaction. *J. Am. Chem. Soc.* **2013**, *135*, 16977−16987.
(28) Xue, Y.; Hui, L.; Yu, H.; Liu, Y.; Fang, Y.; Huang, B.; Zhao, Y.; Li, Z.; Li, Y. Rationally Engineered Active Sites for Efficient and Durable Hydrogen Generation. *Nat. Commun.* **2019**, *10*, 2281.
(29) Sankar, S. S.; Rathishkumar, A.; Geetha, K.; Kundu, S. A Simple Route for the Synthesis of Cobalt Phosphate Nanoparticles for Electrocatalytic Water Oxidation in Alkaline Medium. *Energy Fuels* **2020**, *34*, 12891−12899.
(30) Yuan, C. Z.; Jiang, Y. F.; Wang, Z.; Xie, X.; Yang, Z. K.; Yousaf, A. B.; Xu, A. W. Cobalt Phosphate Nanoparticles Decorated with Nitrogen-Doped Carbon Layers as Highly Active and Stable Electrocatalysts for the Oxygen Evolution Reaction. *J. Mater. Chem. A* **2016**, *4*, 8155−8160.
(31) Koza, J. A.; Hull, C. M.; Liu, Y. C.; Switzer, J. A. Deposition of β-$Co(OH)_2$ Films by Electrochemical Reduction of Tris-(Ethylenediamine)Cobalt(III) in Alkaline Solution. *Chem. Mater.* **2013**, *25*, 1922−1926.
(32) Smith, R. D. L.; Prévot, M. S.; Fagan, R. D.; Trudel, S.; Berlinguette, C. P. Water Oxidation Catalysis: Electrocatalytic Response to Metal Stoichiometry in Amorphous Metal Oxide Films Containing Iron, Cobalt, and Nickel. *J. Am. Chem. Soc.* **2013**, *135*, 11580−11586.
(33) Zhou, J.; Yu, L.; Zhou, Q.; Huang, C.; Zhang, Y.; Yu, B.; Yu, Y. Ultrafast Fabrication of Porous Transition Metal Foams for Efficient Electrocatalytic Water Splitting. *Appl. Catal., B* **2021**, *288*, 120002.
(34) Liu, Y. C.; Koza, J. A.; Switzer, J. A. Conversion of Electrodeposited $Co(OH)_2$ to CoOOH and Co_3O_4, and Comparison of Their Catalytic Activity for the Oxygen Evolution Reaction. *Electrochim. Acta* **2014**, *140*, 359−365.
(35) Hu, J.; Li, S.; Chu, J.; Niu, S.; Wang, J.; Du, Y.; Li, Z.; Han, X.; Xu, P. Understanding the Phase-Induced Electrocatalytic Oxygen Evolution Reaction Activity on FeOOH Nanostructures. *ACS Catal.* **2019**, *9*, 10705−10711.
(36) Dong, G.; Fang, M.; Zhang, J.; Wei, R.; Shu, L.; Liang, X.; Yip, S.; Wang, F.; Guan, L.; Zheng, Z.; Ho, J. C. In Situ Formation of Highly Active Ni-Fe Based Oxygen-Evolving Electrocatalysts via Simple Reactive Dip-Coating. *J. Mater. Chem. A* **2017**, *5*, 11009−11015.
(37) Urbain, F.; Du, R.; Tang, P.; Smirnov, V.; Andreu, T.; Finger, F.; Jimenez Divins, N.; Llorca, J.; Arbiol, J.; Cabot, A.; Morante, J. R. Upscaling high activity oxygen evolution catalysts based on $CoFe_2O_4$ nanoparticles supported on nickel foam for power-to-gas electrochemical conversion with energy efficiencies above 80%. *Appl. Catal., B* **2019**, *259*, 118055.
(38) Nie, J.; Hong, M.; Zhang, X.; Huang, J.; Meng, Q.; Du, C.; Chen, J. 3D Amorphous NiFe LDH Nanosheets Electrodeposited on: In Situ Grown NiCoP@NC on Nickel Foam for Remarkably Enhanced OER Electrocatalytic Performance. *Dalton Trans.* **2020**, *49*, 4896−4903.
(39) Lyons, M. E. G.; Brandon, M. P. The Oxygen Evolution Reaction on Passive Oxide Covered Transition Metal Electrodes in Alkaline Solution. Part III - Iron. *Int. J. Electrochem. Sci.* **2008**, *3*, 1463−1503.
(40) Doyle, R. L.; Lyons, M. E. G. An Electrochemical Impedance Study of the Oxygen Evolution Reaction at Hydrous Iron Oxide in Base. *Phys. Chem. Chem. Phys.* **2013**, *15*, 5224−5237.
(41) Lyons, M. E. G.; Brandon, M. P. The Oxygen Evolution Reaction on Passive Oxide Covered Transition Metal Electrodes in Aqueous Alkaline Solution. Part 1-Nickel. *Int. J. Electrochem. Sci.* **2008**, *3*, 1386−1424.
(42) Han, L.; Tang, P.; Reyes-Carmona, Á.; Rodríguez-García, B.; Torréns, M.; Morante, J. R.; Arbiol, J.; Galan-Mascaros, J. R.

https://doi.org/10.1021/acsaem.3c00032
ACS Appl. Energy Mater. 2023, 6, 5690−5699

Enhanced Activity and Acid pH Stability of Prussian Blue-Type Oxygen Evolution Electrocatalysts Processed by Chemical Etching. *J. Am. Chem. Soc.* **2016**, *138*, 16037−16045.
(43) Exner, K. S.; Over, H. Beyond the Rate-Determining Step in the Oxygen Evolution Reaction over a Single-Crystalline IrO_2(110) Model Electrode: Kinetic Scaling Relations. *ACS Catal.* **2019**, *9*, 6755−6765.
(44) Negahdar, L.; Zeng, F.; Palkovits, S.; Broicher, C.; Palkovits, R. Mechanistic Aspects of the Electrocatalytic Oxygen Evolution Reaction over Ni−Co Oxides. *ChemElectroChem* **2019**, *6*, 5588−5595.

https://doi.org/10.1021/acsaem.3c00032
ACS Appl. Energy Mater. 2023, 6, 5690−5699